THE JOURNAL OF PHYSICAL CHEMISTRY C
A JOURNAL OF THE AMERICAN CHEMICAL SOCIETY

pubs.acs.org/JPCC

Article

Size-Dependent Doping Synergy and Dual-Color Emission in $CsPb_{1-x}Mn_xCl_3$ Nanocrystals

Aaron Forde,* Salim A. Thomas, Reed J. Petersen, Samuel L. Brown, Dmitri S. Kilin, and Erik K. Hobbie*

Cite This: J. Phys. Chem. C 2021, 125, 18849−18856

Read Online

ACCESS | Metrics & More | Article Recommendations | Supporting Information

ABSTRACT: The doping of atomic impurities into colloidal semiconductor nanocrystals (NCs) is a powerful way to tune optical and electronic properties. Manganese (Mn)-doped $CsPbCl_3$ NCs in particular show dual exciton/dopant emission in the visible spectrum, making them materials of current interest for optoelectronic applications. Here, we examine the impact of Mn doping on the photophysics of $CsPbCl_3$ NCs from a different perspective. Using ultracentrifugation, we extract size-resolved fractions from a series of parent NC suspensions prepared at varied doping levels, and we measure the photoresponse as a function of NC size. Our results reveal synergistic radiative effects, with large enhancements in both blue (exciton) and red (dopant) quantum yield (QY) over a narrow range of Mn concentration. We ascribe the first effect to defect passivation and the latter to efficient exciton−dopant charge transfer near a critical point in the number of Mn per NC where the dopant spacing coincides with the Bohr exciton radius. Advanced computational techniques applied to Mn-doped $CsPbCl_3$ reproduce emission colors and concentration trends, with a drop in QY at higher doping levels. Our results offer additional insight into the photophysical interplay of doping, quantum confinement, and radiative relaxation in lead-halide perovskites, while clarifying the complexity of the underlying kinetics and highlighting the critical role of the dopant number per NC at the nanoscale.

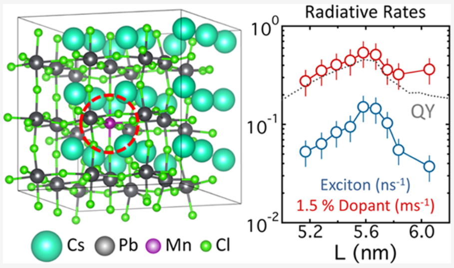

■ INTRODUCTION

The substitutional doping of atomic impurities into semiconducting materials is an effective approach for modifying the electronic transport properties of semiconductors, and the concept of doping serves as the foundation for all of modern solid-state electronics. It is thus not surprising that the impurity doping of nanostructured semiconducting materials has also proven to be an effective way to modify and tune optical and electronic properties at the nanoscale.[1] In the specific case of semiconductor nanocrystals (NCs), recent work demonstrates that the incorporation of atomic impurities—such as transition metals and lanthanides—into the NC lattice can be used to improve intrinsic fluorescence,[2] introduce additional radiative pathways for up-conversion[3,4] or down-conversion,[5,6] or to induce dual-color photoluminescence (PL).[7]

As a timely example of the last effect, efficient Mn^{2+} sensitization leading to two-color emission has recently been observed and studied for wide band gap $CsPb_{1-x}Mn_xCl_3$ lead-halide perovskite (LHP) NCs.[8] These materials exhibit both a fast (1−10 ns)[9] narrow blue emission near 400 nm arising from exciton recombination and a slow (1 ms) broad band orange phosphorescence near 600 nm arising from atomic Mn^{2+} dopants through the spin-forbidden $^4T_1 \rightarrow {}^6A_1$ Mn d−d transition. The Mn^{2+} luminescence is sensitized by the NC exciton through an energy transfer process.[10] Within the LHP lattice, the Mn^{2+} ion is thought to substitute for Pb^{2+} within the octahedral coordination. Due to the Mn^{2+} ion being sensitive to its local environment, the photophysical properties of Mn-doped NCs are expected to depend strongly on concentration,[11−13] the distribution of dopants within the NC lattice,[14] and the degree of electronic confinement, which increases carrier−dopant interactions.[15,16]

Precise control of Mn^{2+} dopant incorporation into the LHP NC lattice is challenging. For hot-injection methods, the reaction kinetics leading to $CsPbX_3$ NC formation are very fast (around 300 ms up to 1 s),[17,18] while the dominance of surface effects at the nanoscale tends to thermodynamically favor dopant exclusion from the NC.[8] Most studies have focused on Mn-doped $CsPbCl_3$ NCs[19,20] because of the difficulty involved in directly incorporating Mn into the $CsPbBr_3$ and $CsPbI_3$ lattice, although one report describes Mn doping of $CsPbBr_3$ in terms of a two-step process.[21] Two different synthetic routes have been used to work past these difficulties: postsynthetic doping of Mn ions into pure $CsPbCl_3$[22−24] and halide

Received: August 6, 2021
Published: August 20, 2021

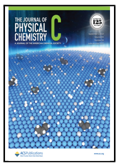

ACS Publications

https://doi.org/10.1021/acs.jpcc.1c06995

exchange reactions for converting $CsPb_{1-x}Mn_xCl_3$ NCs into mixed-halide $CsPb_{1-x}Mn_xCl_{3-y}Br_y$.[8,25,26]

The doping of $CsPbCl_3$ NCs also significantly alters the characteristics of exciton emission. For example, in the low-doping regime, exciton recombination exhibits a significant change in radiative recombination lifetime[23,27,28] coupled with improved PL quantum yield (QY),[29−31] which has been attributed to the shorter Mn-halide bond distance and an increase in the cohesive energy of the lattice.[32] Conversely, in the high-doping regime, there is an anomalous blue shift of the exciton peak,[33,34] where this has been attributed to Ruddlesden−Popper phase defects acting as nanocrystalline grains that induce artificial confinement.[34] Although the Mn^{2+} phosphorescence is largely photostable (insensitive to NC surface defects), it has been observed that there are notable red shifts and decreased PL QY above threshold dopant concentrations. This is generally attributed to antiferromagnetic dopant−dopant interactions that introduce additional nonradiative relaxation pathways,[33] although Auger-like effects may play a role as well.[35,36]

Here, we examine the impact of Mn doping on the photophysics of $CsPbCl_3$ NCs from a unique perspective to get direct physical insight into the underlying radiative and nonradiative processes. Using ultracentrifugation, we extract size-resolved fractions from a series of parent NC suspensions prepared at varied Mn doping levels, and we measure the photoresponse as a function of NC size. Our results reveal synergistic radiative effects associated with dual-color emission, with large enhancements in both blue (exciton) and red (dopant) QY over a narrow range in the number of Mn per NC. We ascribe the first effect to defect passivation by atomic Mn, while the latter effect is attributed to efficient exciton−dopant charge transfer near a critical point in the number of Mn per NC, defined by the mean Mn spacing coinciding with the Bohr exciton radius of $CsPbCl_3$. Of note, we find that the radiative lifetimes, which are typically a quantity that is difficult to engineer, exhibit a minimum (and the corresponding rates a maximum) at this critical point. We interpret this as arising from strong exciton−dopant overlap associated with localization with the anticipated impacts on radiative rates. Advanced computational techniques applied to Mn-doped $CsPbCl_3$ reproduce both emission color and a drop in QY at higher doping levels. Our results offer additional insight into the interplay of doping, quantum confinement, and radiative relaxation in lead-halide perovskites, while highlighting the number of dopants per NC as a critical variable at the nanoscale.

■ RESULTS AND DISCUSSION

Parent Suspensions and Radiative Rates. Details related to NC synthesis can be found in the Supporting Information (SI).[37] We start with doped parent $CsPbCl_3$ NC suspensions synthesized over a range of Mn:Pb feed ratios, with inductively coupled plasma mass spectrometry (ICP-MS) identifying an effective dopant concentration in the $CsPb_{1-x}Mn_xCl_3$ NC lattice that varies from $x = 0$ to 1.5% atomic Mn per Pb. Figure 1 summarizes the dual emission response of the colloidal NCs at varied doping levels. The exciton PL peak near 400 nm is always present but the dopant PL peak near 600 nm does not become significant until a Mn:Pb feed ratio of around 1.0, which translates into x = 0.75% Mn per Pb in the lattice based on ICP-MS. The insets to Figure 1a,c show how the exciton and dopant peaks, respectively, evolve with increased doping, and the inset to Figure 1b shows a schematic of the energy transfer scheme. The slight blue shift in exciton PL with doping is due to the contraction of the $PbCl_6$ octahedra and consequent enhancement of the interaction between Pb and Cl.[33] The overall QY increases up to just below 30% (gray markers, Figure 1e), but more accurately, the exciton QY peaks at around 15% near x = 0.75 to 1.5%, while the dopant QY rises markedly up to around 25% between x = 1 and 1.5%. The increase in exciton QY at low doping levels has been attributed to the removal of structural defects (e.g., chloride vacancies) through the doping process.[31]

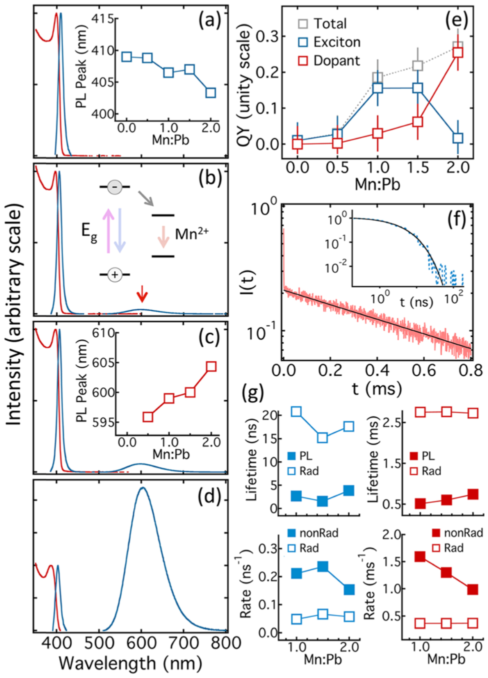

Figure 1. Spectral/lifetime characteristics of parent $CsPb_{1-x}Mn_xCl_3$ NCs as a function of doping level. Absorption (red) and PL (blue) spectra for Mn doping levels of (a) Mn:Pb = 0 (x = 0), (b) Mn:Pb = 1 (x = 0.75%), (c) Mn:Pb = 1.5 (x = 1.1%), and (d) Mn:Pb = 2 (x = 1.5%), where the inset to (a) shows the excitonic PL peak as a function of dopant ratio, the inset to (b) shows a schematic of the energy transfer and dopant emission channel, and the inset to (c) shows the dopant PL peak as a function of Mn:Pb ratio. (e) QY vs dopant ratio showing total QY (gray), excitonic QY (blue), and dopant QY (red). (f) Time-dependent decay of dopant (red) and excitonic (inset, blue) PL for Mn:Pb = 2 (x = 1.5%), where the curves are the fits described in the text. (g) (top) PL and radiative lifetimes for excitonic (left) and dopant (right) emission, and (bottom) radiative and nonradiative rates for excitonic (left) and dopant (right) relaxation.

Because of the large disparity in timescales (six orders of magnitude), the exciton and dopant PL decay channels are easily isolated through spectrally integrated time-correlated photon counting (Figure 1f). Details can be found in the SI. Generally speaking, the exciton PL decay is a stretched-exponential with a 1−10 ns lifetime, while the dopant emission is a single exponential decay with a lifetime near 500 μs. Stretched-exponential decays are indicative of a wide range of relaxation rates,[38,39] as detailed in the SI. Because we independently know the QY of each channel—for brevity referred to as *fast* (exciton) and *slow* (dopant)—we can extract significant information from the lifetime data. The analysis in the SI gives us radiative lifetime from which we derive the radiative and nonradiative rate constants. Specifically, the radiative lifetime for exciton emission is

$$\tau_{f_R} = \left(\frac{\tau_f}{\Phi}\right)\frac{\Gamma(\alpha_f^{-1})}{\alpha_f} \tag{1}$$

where τ_f is exciton lifetime, α_f is the stretching exponent, $\Gamma(x)$ is the gamma function, and $\Phi = \Phi_s + \Phi_f$ is the total QY, while the radiative lifetime for dopant emission is $\tau_{s_R} = \tau_s/\Phi$, where τ_s is the slow PL lifetime. The corresponding radiative rates are $\langle k_{f_R}\rangle = \tau_{f_R}{}^{-1}$ and $k_{s_R} = \tau_{s_R}{}^{-1}$, and from these we deduce the nonradiative rate constants

$$k_{f_{NR}} = \frac{\alpha_f}{\Gamma(\alpha_f^{-1})}\tau_f^{-1} - \tau_{f_R}^{-1} \tag{2}$$

and $k_{s_{NR}} = \tau_s^{-1} - \tau_{s_R}^{-1}$. The relevant quantities are plotted as a function of doping content in Figure 1g.

A comparison of QY (Figure 1e) with the rate constants (lower panels, Figure 1g) suggests that the ratio of radiative to total rate follows the same trend as QY. Looking at radiative and nonradiative rates in the lower panels of Figure 1g, the PL kinetics of both the exciton (left, blue) and dopant (right, red) are consistent with a steady increase in QY with doping, which is linked predominantly to a drop in the nonradiative rate constants. Focusing on exciton QY (blue, Figure 1e), one might expect the opposite trend, but the measurements are indicative of efficient energy transfer and an overall increase in total QY with the added dopant. At the same time, Mn doping enhances the exciton QY, particularly at Mn:Pb ratios of 1.0–1.5 (x = 0.75 to 1.1%) where this enhancement accounts for a large portion of the total increase in QY. This effect has been reported previously and has been attributed to dopant-mediated defect passivation.[33] Here, the data in Figure 1 suggest just a slight rise in $\langle k_{f_R}\rangle$ at maximum QY.

Size-Resolved Measurements. We can gain insight into the nature of the doping profile by performing similar optical measurements on size-resolved NC fractions isolated through density-gradient ultracentrifugation (DGU) in mixed organic solvents.[40−43] Details are given in the SI. NC size as a function of fraction number (depth in the centrifuge tube) is calibrated with transmission electron microscopy (TEM), with typical images shown in Figure 2a and additional images and size histograms presented in Figures S1−S3. By using identical DGU and robotic extraction protocols for each parent, we can map the fraction number onto NC size, with the measured calibration curve presented in Figure S4. The exciton PL peak vs NC edge length (L) is displayed in Figure 2b, while the dopant PL peak vs L is presented in Figure 2c. We obtain a wider emission window through the size separation of just two doped parents (598 to 613 nm, Figure 2c) than what is evident in the parents (595 to 605 nm, inset Figure 1c).

The data suggest that a transition occurs between Mn:Pb ratios of 1.5 and 2.0 (x = 1.1 to 1.5%, respectively). Below this, the exciton PL red-shifts with increasing size, consistent with quantum confinement. Above this, quantum confinement appears to stop at around $L \approx 6.2$ nm, while the dopant emission red-shifts. The first feature is suggestive of Mn impurities inducing defects at higher dopant levels that effectively partition the NCs into subcrystals of smaller size, while the red shift in dopant emission reflects the emergence of dopant−dopant interactions at sufficiently high Mn concentration. For L = 6.2 nm at Mn:Pb = 2 (x = 1.5%), there are roughly 17 Mn atoms per NC, while for Mn:Pb = 1.5 (x = 1.1%), 17 dopants per NC corresponds to a slightly larger length scale of around 6.9 nm, which is where a similar plateau starts to emerge for Mn:Pb = 1.5, as shown in Figure 2b. Despite these trends, TEM revealed no significant evidence of defects for NCs in this size range (4−7 nm), although we anticipate that such trends would be difficult to discern at these NC sizes and doping levels.[34]

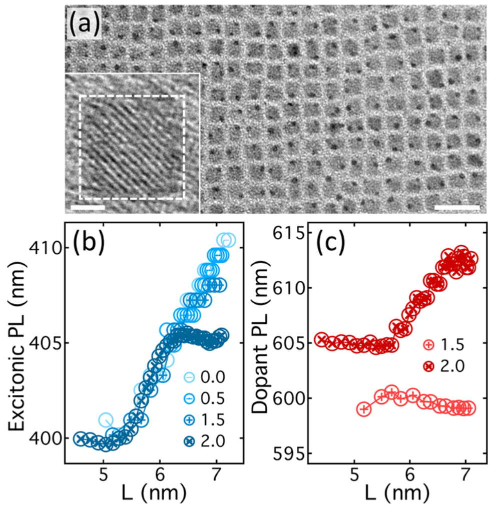

Figure 2. TEM images of (a) 2D NC superlattice for Mn:Pb = 1.5 (x = 1.1%, f35, 20 nm scale), where the inset shows an individual NC for Mn:Pb = 2.0 (x = 1.5%, f18, 2 nm scale). (b) Excitonic PL peak vs edge length for size-separated NCs extracted from parents of a varied dopant feed ratio, and (c) similar plot for the red dopant emission. Marker labels in the plots indicate the Mn:Pb feed ratio.

The QY as a function of NC size at varied doping levels sheds additional light on the picture, with the first example summarized in Figure 3 (Mn:Pb = 1.5, or x = 1.1%). Excitonic emission is strong for these fractions, but weak dopant PL is present as well (Figure 3a). Overall, with the exception of a slight dip near L = 6 nm, the QY increases with increasing size, falling naturally into the three labeled size regimes. Although fractions were rejuvenated with additional ligands post DGU, the QY of the fractions is slightly below that of the parent (Figure 3b), which we attribute to the interval during/after size separation where the NCs resided in a ligand-depleted environment.[40] Nonetheless, the exciton emission is much stronger in the doped fractions, compared to undoped $CsPbCl_3$, and it dominates the total QY (Figure 3c). Figure 3d highlights the trend of increasing QY with increasing size for the three regions in Figure 3b.

At just slightly higher doping levels (Mn:Pb = 2, x = 1.5%), the behavior is quite different (Figure 4). Now, the PL is dominated by the dopant (Figure 4a), with a maximum QY of 45% near L = 5.6 nm, which is well above that of the parent (Figure 4b). The data again split naturally into three size regimes (Figure 4b), but with different boundaries than those shown in Figure 3. The dopant emission now dominates the QY, with excitonic emission comparable to or below that of pure $CsPbCl_3$ NCs (Figure 4c). Notably, both contributions to QY exhibit a peak near L = 5.6 nm, and in contrast to the behavior in Figure 3d, the QY first increases but then decreases with increasing NC size, more sharply at larger sizes.

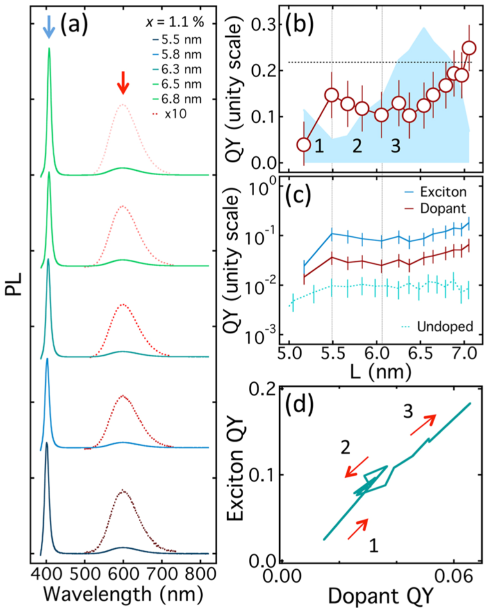

Figure 3. PL characteristics of size-fractionated $\mathrm{CsPb}_{1-x}\mathrm{Mn}_x\mathrm{Cl}_3$ NCs prepared at Mn:Pb = 1.5 (x = 1.1%). (a) PL spectra for the indicated edge length, where the dopant emission peak has been multiplied by a factor of 10 for clarity. (b) Total PL QY, where the horizontal dashed line indicates QY of the parent suspension and the shaded blue background is the absorption intensity. (c) Dopant (red) and exciton (blue, doped/undoped) PL QY as a function of NC size. (d) Exciton QY vs dopant QY. The three different size regimes discussed in the text are delineated.

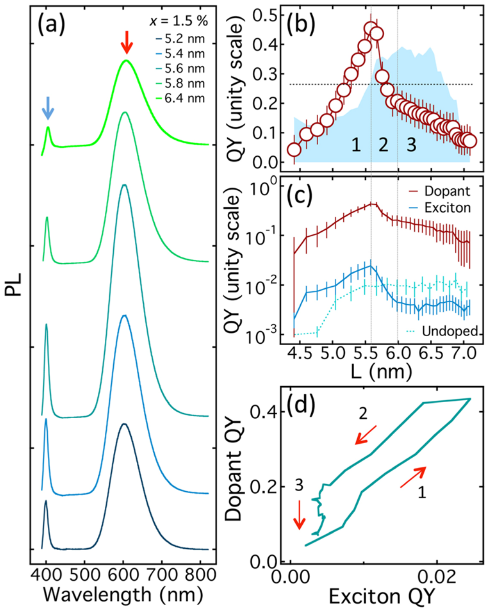

Figure 4. PL characteristics of size-fractionated $\mathrm{CsPb}_{1-x}\mathrm{Mn}_x\mathrm{Cl}_3$ NCs prepared at Mn:Pb = 2.0 (x = 1.5%). (a) PL spectra for the indicated edge length. (b) Total PL QY, where the horizontal dashed line indicates QY of the parent suspension and the shaded blue background is the absorption measured in an integrating sphere. (c) Dopant (red) and exciton (blue, doped/undoped) PL QY as a function of NC size. (d) Exciton QY vs dopant QY. The three different size regimes discussed in the text are delineated.

The final and most critical piece of information is PL relaxation. The PL decays for the fractions exhibit the same temporal trends as the parents: stretched-exponential decays for the excitonic channel and single exponential decays for the dopant channel, with the description of the rate constants derived above. Representative decay curves and additional analysis can be found in the SI (Figure S4). Focusing first on modest doping (Mn:Pb = 1.5, x = 1.1%, Figure 5a,b), there are two trends of note in the excitonic decay constants. First, in comparison to Figure 3b, we see that the increase in QY with size (the majority of the mass distribution in Figure 3b) is simply due to a drop in the nonradiative rate constant (region 3, Figure 5b), where the radiative rate drops only slightly over the same size range. Defect passivation by Mn is thus the root cause of the increase in excitonic QY (see also Figure 1e), while both rates (radiative and nonradiative) exhibit a peak and both lifetimes a minimum, where the QY in Figure 3b is a minimum ($L \approx 6$ nm). This peak represents the optimal NC size, at a given Mn concentration, for efficient exciton−dopant energy transfer.

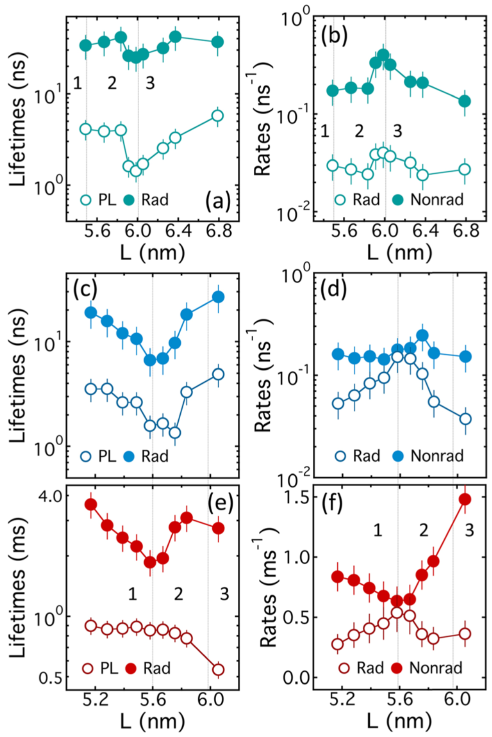

Figure 5. Photoluminescence lifetimes and the associated rate constants for size-fractionated $\mathrm{CsPb}_{1-x}\mathrm{Mn}_x\mathrm{Cl}_3$ NCs derived from parents with Mn:Pb = 1.5 (x = 1.1%) (a and b) and Mn:Pb = 2.0 (x = 1.5%) (c−f). The plots on the left show both PL and radiative lifetime vs size, while those on the right show the radiative and nonradiative rate vs size. Dopant emission is indicated in red. The size regimes delineated in Figures 3 and 4 are included.

This picture is further supported by the PL relaxation response at Mn:Pb = 2 (x = 1.5%, Figure 5c−f), where the excitonic lifetime now exhibits a minimum near $L \approx 5.6$ nm (Figure 5c) where QY exhibits a maximum (Figure 4c). This trend is also evident as a peak in the excitonic radiative rate but with a nonradiative rate that is relatively flat (Figure 5d). However, the radiative lifetime for dopant emission now also exhibits a minimum near $L \approx 5.6$ nm, leading to the unusual behavior shown in Figure 5f, where k_{s_R} exhibits a maximum at the same point where $k_{s_{NR}}$ shows a minimum. The PL response

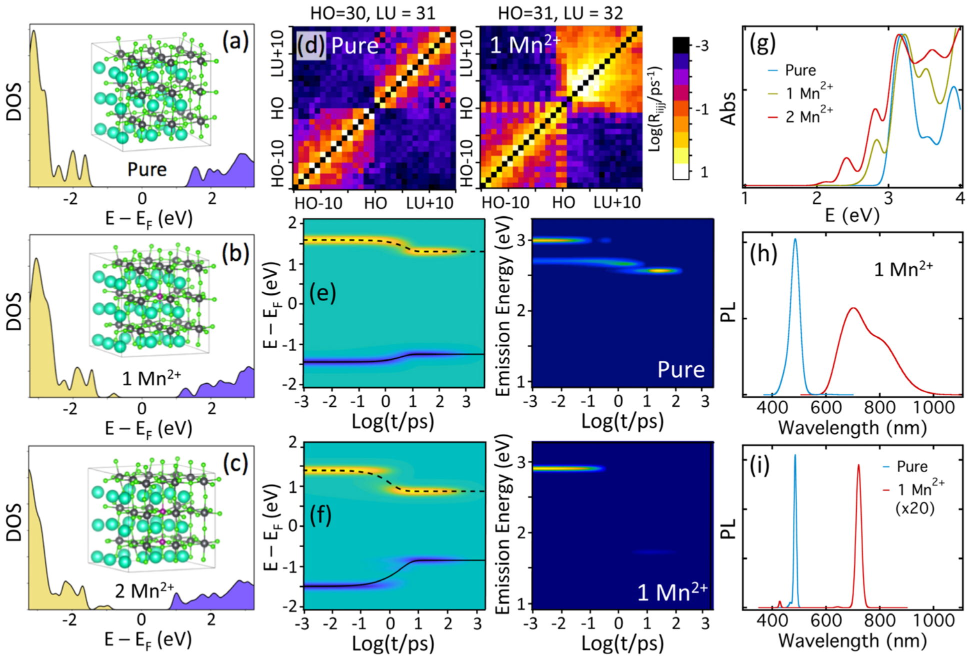

Figure 6. Computational results based on DFT and nonadiabatic excited-state dynamics simulations. (a−c) DOS computed for LHP with (a) no dopants, (b) 1 Mn^{2+} dopant, and (c) 2 Mn^{2+} dopants. Insets show the atomistic structures with Pb = gray, Mn = purple, and Cl = green. (d) Redfield tensor elements R_{iijj} for the pure (left) and doped (right) scenarios. (e) Nonradiative (left) and radiative (right) relaxation kinetics for the pure lattice. (f) Nonradiative (left) and radiative (right) relaxation kinetics for the doped lattice. (g) Absorption spectra based on DFT for the three scenarios in (a−c). (h) Thermally broadened excitonic (blue) and dopant (red) PL spectra computed from DFT for the single dopant scenario. (i) Time-integrated PL from nonadiabatic excited-state dynamics simulations for the pure and doped lattice.

here is dominated by energy transfer (as opposed to passivation), with the majority of radiative relaxation dumped into the dopant emission channel. The critical NC sizes for the peak exciton radiative rates (6 nm for $x = 1.1\%$ and 5.6 nm for $x = 1.5\%$) suggest a decrease in critical size with increased doping, consistent with $(5.6)^3/(6)^3 \approx 1.1/1.5$, where the peak in the radiative rate occurs at around 13 Mn per NC in each case. Note that the transition described here, which is associated with a type of radiative resonance, is distinct from that shown in Figure 2, which represents the onset of strong doping at slightly larger size and a subsequent drop in QY.

Because the dopant emission exhibits a pure exponential decay, we can assume that Mn is uniformly distributed.[37] In a Dexter-type energy transfer scheme mediated by phonons, the exciton needs to be strongly localized around the dopant for energy transfer to be efficient,[44] and because the radiative rate scales as the square of the dipole matrix element, strong exciton/dopant overlap is critical for maximizing radiative relaxation. Based on this, we can understand the measured trends through a simple scaling argument. Let N denote the number of dopants per NC, with $n = N/L^3$ being the density. For a given L, there is a critical dopant number $N_c = n_c L^3$, where $n_c \propto R_B^{-3}$ is the critical density and $R_B \approx 2.5$ nm is the exciton Bohr radius of $CsPbCl_3$.[17] At the critical point, the NC has the optimal number of dopants: below this threshold there is unutilized volume, while above this threshold dopant−dopant interactions start to emerge. Assuming a mean size of $L = 6$ nm for a parent suspension, the critical dopant number is $N_c \approx 14$, which occurs at $x = 1.4\%$ (Mn:Pb = 1.8), in agreement with the trends shown in Figure 1e. The primary handle for establishing optimum exciton−dopant energy transfer, or "resonance", is thus dopant density. However, for NCs of arbitrary size and density not far removed from the critical point, we can use N_c as a point of reference through $nL^3 = N_c$. For densities slightly below n_c, for example, we will find resonance at the slightly larger critical size $L_c \propto (N_c/n)^{1/3}$, which explains the trends discussed in the previous paragraph.

Quantum Simulations. For additional insight, we implement density functional theory (DFT) to model radiative and nonradiative relaxation processes, where details of the methodology can be found in the SI. We investigate three atomistic models (insets, Figure 6a−c): a pristine $CsPbCl_3$ bulk lattice, a model with one Mn^{2+} dopant replacing the central Pb^{2+}, and a model with two Mn^{2+} dopants connected by a Cl^- bridge. For each, we compute the ground-state electronic structure in a spin-polarized basis to account for the open-shell nature of Mn^{2+} ions. We find that for one Mn^{2+} dopant, the lowest energy spin multiplicity is the ferromagnetic $S = 5/2$ configuration, while with two dopants the antiferromagnetic $S = 0$ configuration is the ground state. From the spin-polarized ground-state electronic configuration, we compute the electronic structure in the basis of spinor Kohn-Sham orbitals with spin−orbit coupling, where the latter is crucial to the radiative properties of Mn^{2+} complexes. Figure 6a−c shows the computed density of states (DOS), where additional electronic states are introduced inside the pristine $CsPbCl_3$ band gap upon doping. Visual inspection of the charge densities (Figures S7 and S8) reveals that these additional states are Mn^{2+} 3d orbitals localized on the dopant site. This gives the expected qualitative trend of Mn^{2+} electronic states residing inside the LHP band gap, enabling dopant luminescence. Figure 6g shows computed absorption spectra for each scenario, demonstrating how Mn−Mn interactions red-shift the band edge, which is in qualitative agreement with Figures 1c and 2e.

For excited-state dynamics, we compute "on-the-fly" nonadiabatic couplings along a molecular dynamics (MD) trajectory for both pristine $CsPbCl_3$ and the lattice with one Mn^{2+} dopant. The data are processed into Redfield tensors (Figure 6d), which represent nonradiative state-to-state transition rates. The electronic states associated with the dopant (Figure 6b) show strong coupling to the LHP lattice, as evidenced by the emergence of off-diagonal elements in Figure 6d. Figure 6e,f shows the time-resolved nonradiative (left) and radiative (right) dynamics for the pristine and doped models. For the nonradiative decay, yellow (blue) represents the negative (positive) charge density of the electron (hole), with the dashed (solid) curve showing the electron (hole) energy expectation value. There is clear nonradiative relaxation induced by the dopant. Table S2 summarizes the carrier cooling rates $k_{e/h}$ to the lowest unoccupied (LU) and highest occupied (HO) states.

For the radiative dynamics (right panels), the dark blue background represents optically dark states while the yellow and light blue regions represent emission. Integrated PL spectra (Figure 6i) for the pristine model show exciton emission (blue), while the doped model (red) shows dual emission features: high intensity "red" dopant emission and low intensity "blue" exciton emission from the LHP. Table S2 also summarizes the radiative and nonradiative recombination rates, k_R and k_{NR}, respectively, and the resultant PL QY. The PL linewidths from Figure 6e,f are artificially narrow, and to account for electron−phonon coupling we implement MDPL plots of oscillator strengths along the MD trajectory, as shown in Figure 6h, for the pristine (blue) and doped lattice (red). The linewidths qualitatively agree with the experiment, with the LHP showing a narrower band and the dopant showing broad band PL extending into the NIR. We emphasize that 1 Mn per cell in the simulations corresponds to $x = 3.8\%$. This is 2× larger than the highest experimental values, and the simulated QY is thus consistent with the large-size tail shown in Figure 4b and the associated drop in QY. However, the current simulations cannot capture the radiative charge transfer revealed by the experiments in Figures 4 and 5, with the main obstacle being system size: a much larger simulation would be needed to capture relaxation at the relevant and relatively low dopant concentrations where resonance is expected to occur.

CONCLUSIONS

In conclusion, we have studied the impact of Mn doping on the radiative emission of $CsPbCl_3$ NCs from the unique perspective of both NC size and dopant concentration. We find dual synergistic radiative effects, with large enhancements in both QYs (blue/exciton and red/dopant) over narrow ranges of size and doping levels. Exciton emission is enhanced at weak doping through defect passivation, while dopant emission is enhanced at modest doping through exciton−dopant energy transfer. Our measurements reveal that the latter effect occurs at a critical point in the number of dopant atoms per NC or where the Mn spacing roughly coincides with the exciton Bohr radius of $CsPbCl_3$. While both effects are evident in parent suspensions queried as a function of the doping level, they become more detailed in size-resolved fractions derived from parent suspensions prepared at varied doping density. Advanced computational techniques applied to Mn-doped $CsPbCl_3$ in the high-doping limit are able reproduce the dual emission trends, with emission dominated by the dopant channel at high-doping levels. Our results offer unique additional insight into the photophysical interplay of doping, quantum confinement, and radiative relaxation in LHPs, while clarifying the complexity of the underlying kinetics. In particular, our results emphasize the critical role of the dopant number per NC at the nanoscale, while demonstrating a system where optimal QY is governed by the emergence of radiative processes in addition to the suppression of nonradiative channels.

ASSOCIATED CONTENT

Supporting Information

The Supporting Information is available free of charge at https://pubs.acs.org/doi/10.1021/acs.jpcc.1c06995.

Description of doped NC synthesis/processing, DGU size separation, TEM size distributions, descriptions of the experimental approach/methods, and an in-depth discussion of the computational modeling (PDF)

AUTHOR INFORMATION

Corresponding Authors

Aaron Forde − *Materials and Nanotechnology Program, North Dakota State University, Fargo, North Dakota 58108, United States*; Email: aaron.forde@ndsu.edu

Erik K. Hobbie − *Materials and Nanotechnology Program, Department of Physics, and Department of Coatings and Polymeric Materials, North Dakota State University, Fargo, North Dakota 58108, United States*; orcid.org/0000-0001-6158-8977; Email: erik.hobbie@ndsu.edu

Authors

Salim A. Thomas − *Materials and Nanotechnology Program, North Dakota State University, Fargo, North Dakota 58108, United States*

Reed J. Petersen − *Department of Physics, North Dakota State University, Fargo, North Dakota 58108, United States*

Samuel L. Brown − *Materials and Nanotechnology Program, North Dakota State University, Fargo, North Dakota 58108, United States*

Dmitri S. Kilin − *Materials and Nanotechnology Program and Department of Chemistry and Biochemistry, North Dakota State University, Fargo, North Dakota 58108, United States*; orcid.org/0000-0001-7847-5549

Complete contact information is available at: https://pubs.acs.org/10.1021/acs.jpcc.1c06995

Notes

The authors declare no competing financial interest.

ACKNOWLEDGMENTS

E.K.H. acknowledges support from the National Science Foundation (NSF) through CBET-1603445 and D.K. acknowledges the support of NSF CHE-1944921. The authors also acknowledge the support of the Department of Energy (DOE) under contract DEAC02-05CH11231.

REFERENCES

(1) Norris, D. J.; Efros, A. L.; Erwin, S. C. Doped Nanocrystals. *Science* **2008**, *319*, 1776−1779.

(2) Sahu, A.; Kang, M. S.; Kompch, A.; Notthoff, C.; Wills, A. W.; Deng, D.; Winterer, M.; Frisbie, C. D.; Norris, D. J. Electronic Impurity Doping in CdSe Nanocrystals. *Nano Lett.* **2012**, *12*, 2587−2594.

(3) Kramer, K. W.; Biner, D.; Frei, G.; Gudel, H. U.; Hehlen, M. P.; Luthi, S. R. Hexagonal Sodium Yttrium Fluoride Based Green and Blue Emitting Upconversion Phosphors. *Chem. Mater.* **2004**, *16*, 1244−1251.

(4) Zhang, F.; Wan, Y.; Yu, T.; Zhang, F.; Shi, Y.; Xie, S.; Li, Y.; Xu, L.; Tu, B.; Zhao, D. Uniform Nanostructured Arrays of Sodium Rare-Earth Fluorides for Highly Efficient Multicolor Upconversion Luminescence. *Angew. Chem., Int. Ed.* **2007**, *46*, 7976−7979.

(5) Soo, Y. L.; Ming, Z. H.; Huang, S. W.; Kao, Y. H.; Bhargava, R. N.; Gallagher, D. Local Structures around Mn Luminescent Centers in Mn-Doped Nanocrystals of ZnS. *Phys. Rev. B* **1994**, *50*, 7602−7607.

(6) Milstein, T. J.; Kroupa, D. M.; Gamelin, D. R. Picosecond Quantum Cutting Generates Photoluminescence Quantum Yields over 100% in Ytterbium-Doped $CsPbCl_3$ Nanocrystals. *Nano Lett.* **2018**, *18*, 3792−3799.

(7) Vlaskin, V. A.; Janssen, N.; van Rijssel, J.; Beaulac, R.; Gamelin, D. R. Tunable Dual Emission in Doped Semiconductor Nanocrystals. *Nano Lett.* **2010**, *10*, 3670−3674.

(8) Liu, W.; Lin, Q.; Li, H.; Wu, K.; Robel, I.; Pietryga, J. M.; Klimov, V. I. Mn^{2+}-Doped Lead Halide Perovskite Nanocrystals with Dual-Color Emission Controlled by Halide Content. *J. Am. Chem. Soc.* **2016**, *138*, 14954−14961.

(9) Becker, M. A.; Vaxenburg, R.; Nedelcu, G.; Sercel, P. C.; Shabaev, A.; Mehl, M. J.; Michopoulos, J. G.; Lambrakos, S. G.; Bernstein, N.; Lyons, J. L.; Stöferle, T.; Mahrt, R. F.; Kovalenko, M. V.; Norris, D. J.; Rainò, G.; Efros, A. L. Bright Triplet Excitons in Caesium Lead Halide Perovskites. *Nature* **2018**, *553*, 189−193.

(10) Parobek, D.; Roman, B. J.; Dong, Y.; Jin, H.; Lee, E.; Sheldon, M.; Son, D. H. Exciton-to-Dopant Energy Transfer in Mn-Doped Cesium Lead Halide Perovskite Nanocrystals. *Nano Lett.* **2016**, *16*, 7376−7380.

(11) Vink, A. P.; de Bruin, M. A.; Roke, S.; Peijzel, P. S.; Meijerink, A. Luminescence of Exchange Coupled Pairs of Transition Metal Ions. *J. Electrochem. Soc.* **2001**, *148*, No. E313.

(12) Norris, D. J.; Yao, N.; Charnock, F. T.; Kennedy, T. A. High-Quality Manganese-Doped ZnSe Nanocrystals. *Nano Lett.* **2001**, *1*, 3−7.

(13) Zhu, J.; Yang, X.; Zhu, Y.; Wang, Y.; Cai, J.; Shen, J.; Sun, L.; Li, C. Room-Temperature Synthesis of Mn-Doped Cesium Lead Halide Quantum Dots with High Mn Substitution Ratio. *J. Phys. Chem. Lett.* **2017**, *8*, 4167−4171.

(14) Chen, H.-Y.; Maiti, S.; Son, D. H. Doping Location-Dependent Energy Transfer Dynamics in Mn-Doped CdS/ZnS Nanocrystals. *ACS Nano* **2012**, *6*, 583−591.

(15) Hoffman, D. M.; Meyer, B. K.; Ekimov, A. I.; Merkulov, I. A.; Efros, A. L.; Rosen, M.; Couino, G.; Gacoin, T.; Boilot, J. P. Giant Internal Magnetic Fields in Mn Doped Nanocrystal Quantum Dots. *Solid State Commun.* **2000**, *114*, 547−550.

(16) Fainblat, R.; Barrows, C. J.; Gamelin, D. R. Single Magnetic Impurities in Colloidal Quantum Dots and Magic-Size Clusters. *Chem. Mater.* **2017**, *29*, 8023−8036.

(17) Protesescu, L.; Yakunin, S.; Bodnarchuk, M. I.; Krieg, F.; Caputo, R.; Hendon, C. H.; Yang, R. X.; Walsh, A.; Kovalenko, M. V. Nanocrystals of Cesium Lead Halide Perovskites ($CsPbX_3$, X = Cl, Br, and I): Novel Optoelectronic Materials Showing Bright Emission with Wide Color Gamut. *Nano Lett.* **2015**, *15*, 3692−3696.

(18) Lignos, I.; Stavrakis, S.; Nedelcu, G.; Protesescu, L.; deMello, A. J.; Kovalenko, M. V. Synthesis of Cesium Lead Halide Perovskite Nanocrystals in a Droplet-Based Microfluidic Platform: Fast Parametric Space Mapping. *Nano Lett.* **2016**, *16*, 1869−1877.

(19) Mir, W. J.; Jagadeeswararao, M.; Das, S.; Nag, A. Colloidal Mn-Doped Cesium Lead Halide Perovskite Nanoplatelets. *ACS Energy Lett.* **2017**, *2*, 537−543.

(20) Biswas, A.; Bakthavatsalam, R.; Kundu, J. Efficient Exciton to Dopant Energy Transfer in Mn^{2+}-Doped $(C_4H_9NH_3)_2PbBr_4$ Two-Dimensional (2d) Layered Perovskites. *Chem. Mater.* **2017**, *29*, 7816−7825.

(21) Parobek, D.; Dong, Y.; Qiao, T.; Son, D. H. Direct Hot-Injection Synthesis of Mn-Doped $CsPbBr_3$ Nanocrystals. *Chem. Mater.* **2018**, *30*, 2939−2944.

(22) Qiao, T.; Parobek, D.; Dong, Y.; Ha, E.; Son, D. H. Photoinduced Mn Doping in Cesium Lead Halide Perovskite Nanocrystals. *Nanoscale* **2019**, *11*, 5247−5253.

(23) Mir, W. J.; Mahor, Y.; Lohar, A.; Jagadeeswararao, M.; Das, S.; Mahamuni, S.; Nag, A. Postsynthesis Doping of Mn and Yb into CsPbX3 (X = Cl, Br, or I) Perovskite Nanocrystals for Down-conversion Emission. *Chem. Mater.* **2018**, *30*, 8170−8178.

(24) Lin, C. C.; Xu, K. Y.; Wang, D.; Meijerink, A. Luminescent Manganese-Doped $CsPbCl_3$ Perovskite Quantum Dots. *Sci. Rep.* **2017**, *7*, 45906.

(25) De Siena, M. C.; Sommer, D. E.; Creutz, S. E.; Dunham, S. T.; Gamelin, D. R. Spinodal Decomposition During Anion Exchange in Colloidal Mn^{2+}-Doped $CsPbX_3$ (X = Cl, Br) Perovskite Nanocrystals. *Chem. Mater.* **2019**, *31*, 7711−7722.

(26) Xu, K.; Meijerink, A. Tuning Exciton−Mn^{2+} Energy Transfer in Mixed Halide Perovskite Nanocrystals. *Chem. Mater.* **2018**, *30*, 5346−5352.

(27) Hou, S.; Gangishetty, M. K.; Quan, Q.; Congreve, D. N. Efficient Blue and White Perovskite Light-Emitting Diodes *via* Manganese Doping. *Joule* **2018**, *2*, 2421−2433.

(28) Zou, S.; Liu, Y.; Li, J.; Liu, C.; Feng, R.; Jiang, F.; Li, Y.; Song, J.; Zeng, H.; Hong, M.; Chen, X. Stabilizing Cesium Lead Halide Perovskite Lattice through Mn(II) Substitution for Air-Stable Light-Emitting Diodes. *J. Am. Chem. Soc.* **2017**, *139*, 11443−11450.

(29) Mondal, N.; De, A.; Samanta, A. Achieving near-Unity Photoluminescence Efficiency for Blue-Violet-Emitting Perovskite Nanocrystals. *ACS Energy Lett.* **2019**, *4*, 32−39.

(30) Bi, C.; Wang, S.; Li, Q.; Kershaw, S. V.; Tian, J.; Rogach, A. L. Thermally Stable Copper(Ii)-Doped Cesium Lead Halide Perovskite Quantum Dots with Strong Blue Emission. *J. Phys. Chem. Lett.* **2019**, *10*, 943−952.

(31) Yong, Z.-J.; Guo, S.-Q.; Ma, J.-P.; Zhang, J.-Y.; Li, Z.-Y.; Chen, Y.-M.; Zhang, B.-B.; Zhou, Y.; Shu, J.; Gu, J.-L.; Zheng, L.-R.; Bakr, O. M.; Sun, H.-T. Doping-Enhanced Short-Range Order of Perovskite Nanocrystals for near-Unity Violet Luminescence Quantum Yield. *J. Am. Chem. Soc.* **2018**, *140*, 9942−9951.

(32) Akkerman, Q. A.; Meggiolaro, D.; Dang, Z.; De Angelis, F.; Manna, L. Fluorescent Alloy $CsPb_xMn_{1-x}I_3$ Perovskite Nanocrystals with High Structural and Optical Stability. *ACS Energy Lett.* **2017**, *2*, 2183−2186.

(33) De, A.; Mondal, N.; Samanta, A. Luminescence Tuning and Exciton Dynamics of Mn-Doped $CsPbCl_3$ Nanocrystals. *Nanoscale* **2017**, *9*, 16722−16727.

(34) Paul, S.; Bladt, E.; Richter, A. F.; Döblinger, M.; Tong, Y.; Huang, H.; Dey, A.; Bals, S.; Debnath, T.; Polavarapu, L.; Feldmann, J. Manganese-Doping-Induced Quantum Confinement within Host Perovskite Nanocrystals through Ruddlesden−Popper Defects. *Angew. Chem., Int. Ed.* **2020**, *59*, 6794−6799.

(35) Wang, S.; Leng, J.; Yin, Y.; Liu, J.; Wu, K.; Jin, S. Ultrafast Dopant-Induced Exciton Auger-like Recombination in Mn-Doped Perovskite Nanocrystals. *ACS Energy Lett.* **2020**, *5*, 328−334.

(36) Sun, Q.; Wang, S.; Zhao, C.; Leng, J.; Tian, W.; Jin, S. Excitation-Dependent Emission Color Tuning from an Individual Mn-Doped Perovskite Microcrystal. *J. Am. Chem. Soc.* **2019**, *141*, 20089−20096.

(37) Yuan, X.; Ji, S.; De Siena, M. C.; Fei, L.; Zhao, Z.; Wang, Y.; Li, H.; Zhao, J.; Gamelin, D. R. Photoluminescence Temperature Dependence, Dynamics, and Quantum Efficiencies in Mn^{2+}-Doped $CsPbCl_3$ Perovskite Nanocrystals with Varied Dopant Concentration. *Chem. Mater.* **2017**, *29*, 8003−8011.

(38) Brown, S. L.; Krishnan, R.; Elbaradei, A.; Sivaguru, J.; Sibi, M. P.; Hobbie, E. K. Origin of Stretched-Exponential Photoluminescence Relaxation in Size-Separated Silicon Nanocrystals. *AIP Adv.* **2017**, *7*, No. 055314.

(39) van Driel, A. F.; Nikolaev, I. S.; Vergeer, P.; Lodahl, P.; Vanmaekelbergh, D.; Vos, W. L. Statistical Analysis of Time-Resolved

Emission from Ensembles of Semiconductor Quantum Dots: Interpretation of Exponential Decay Models. *Phys. Rev. B* **2007**, *75*, No. 035329.

(40) Forde, A.; Fagan, J. A.; Schaller, R. D.; Thomas, S. A.; Brown, S. L.; Kurtti, M. B.; Petersen, R. J.; Kilin, D. S.; Hobbie, E. K. Brightly Luminescent $CsPbBr_3$ Nanocrystals through Ultracentrifugation. *J. Phys. Chem. Lett.* **2020**, *11*, 7133−7140.

(41) Pringle, T. A.; Hunter, K. I.; Brumberg, A.; Anderson, K. J.; Fagan, J. A.; Thomas, S. A.; Petersen, R. J.; Sefannaser, M.; Han, Y.; Brown, S. L.; Kilin, D. S.; Schaller, R. D.; Kortshagen, U. R.; Boudjouk, P. R.; Hobbie, E. K. Bright Silicon Nanocrystals from a Liquid Precursor: Quasi-Direct Recombination with High Quantum Yield. *ACS Nano* **2020**, *14*, 3858−3867.

(42) Miller, J. B.; Harris, J. M.; Hobbie, E. K. Purifying Colloidal Nanoparticles through Ultracentrifugation with Implications for Interfaces and Materials. *Langmuir* **2014**, *30*, 7936−7946.

(43) Miller, J. B.; Hobbie, E. K. Nanoparticles as Macromolecules. *J. Polym. Sci., Part B: Polym. Phys.* **2013**, *51*, 1195−1208.

(44) Dexter, D. L. A Theory of Sensitized Luminescence in Solids. *J. Chem. Phys.* **1953**, *21*, 836−850.

https://doi.org/10.1021/acs.jpcc.1c06995
J. Phys. Chem. C 2021, 125, 18849−18856